

Enhancement of radiation detection performance with reduction of $\text{EH}_{6/7}$ deep levels in n-type 4H-SiC through thermal oxidation

Cite as: Appl. Phys. Lett. **121**, 012103 (2022); doi: [10.1063/5.0089236](https://doi.org/10.1063/5.0089236)

Submitted: 24 February 2022 · Accepted: 17 June 2022 ·

Published Online: 5 July 2022



View Online



Export Citation



CrossMark

OmerFaruk Karadavut,  Sandeep K. Chaudhuri,  Joshua W. Kleppinger, Ritwik Nag, and Krishna C. Mandal^{a)} 

AFFILIATIONS

Department of Electrical Engineering, University of South Carolina, Columbia, South Carolina 29208, USA

^{a)} Author to whom correspondence should be addressed: mandalk@cec.sc.edu. Tel.: +1 (803) 777-2722

ABSTRACT

We report the effect of $\text{EH}_{6/7}$ electron trap centers alone on the performance of high-resolution radiation detectors fabricated on n-type 4H-SiC epitaxial layers. A Schottky barrier detector (SBD) and a metal-oxide-semiconductor (MOS) capacitor detector fabricated using two sister samples derived from the same 50 μm 4H-SiC parent wafer exhibited widely different energy resolutions of 0.4% and 0.9% for 5486 keV alpha particles. An equivalent noise charge model analysis ruled out the effect of the detector capacitance and the leakage current on the resolution of the detectors. Deep level transient spectroscopic studies revealed the presence of two trapping centers in each detector within the temperature scan range 240–800 K. The $\text{Z}_{1/2}$ center, a potential electron trap, was detected in both the detectors in equal concentration, which suggested that the observed difference in the energy resolution is due to the presence of the other defect, the $\text{EH}_{6/7}$ center, in the SBD. The capture cross section of the $\text{EH}_{6/7}$ center was calculated to be three orders of magnitude higher than the second defect [a carbon antisite vacancy (CAV) center] observed in the MOS detector with an activation energy of 1.10 eV, which accounted for the enhanced electronic trapping in the SBD leading to its poor energy resolution. It has been proposed that the $\text{EH}_{6/7}$ centers in the SBD have likely been reconfigured to CAV pairs during the thermal growth of the silicon dioxide layer in the MOS detector. The proposed formation mechanism of CAV, a stable qubit state for quantum information processing, addresses the outstanding questions related to the role of defect dynamics in their formation.

Published under an exclusive license by AIP Publishing. <https://doi.org/10.1063/5.0089236>

Research on wide bandgap (WBG) semiconductors for high-temperature, high-power, high-frequency, and harsh environment applications has tremendously escalated in the recent years as the advancement in growth technologies has demonstrated superior charge transport properties in these materials.^{1–4} Charge transport properties are one of the most important factors that define the electronic performance of semiconductor devices.^{5,6} WBG semiconductors are also ideal for radiation detection at room and higher temperatures as they exhibit extremely low leakage currents at elevated temperatures.^{7–10} Among various WBG semiconductors such as single crystalline diamond (5.45 eV), Ga_2O_3 (4.8 eV), and GaN (3.4 eV), 4H-SiC with a bandgap of 3.26 eV has advanced the most in terms of low-cost, high-purity, and large area single crystal growth.^{11–13} Presently, epitaxially grown 4H-SiC layers with thickness up to 250 μm and a wafer diameter of 100 mm are regularly grown, which exhibit areal micropipe defect density less than 1 cm^{-2} and deep level trap concentration on the order of 10^{11} cm^{-3} .^{14,15}

Being extremely radiation hard, 4H-SiC is the sole choice for high resolution radiation detection in extreme radiation environments.^{16,17} Yet another important factor required in high resolution detector materials is low electron-hole pair (ehp) creation energy, which ensures a higher number of radiation-induced charge pairs and, hence, lower Fano noise even for very low energy radiations.¹⁸ The ehp creation energy in semiconductors is roughly three times the bandgap energy. Thus, even though a wide bandgap ensures low leakage current, ultrawide bandgap materials may lead to deterioration of the energy resolution. The ehp creation energy in 4H-SiC is reported to be 7.78 eV,¹⁹ which is favorably low for detecting x rays and low energy γ rays.⁸ Also, 4H-SiC is the only WBG semiconductor that has SiO_2 as its native oxide layer, which makes it compatible to the standard metal-oxide-semiconductor (MOS) device fabrication procedures.²⁰ Vertical Schottky barrier detector (SBD) geometry is the most preferred configuration for high resolution radiation detection, which is readily obtained by depositing metal contacts on the silicon face of

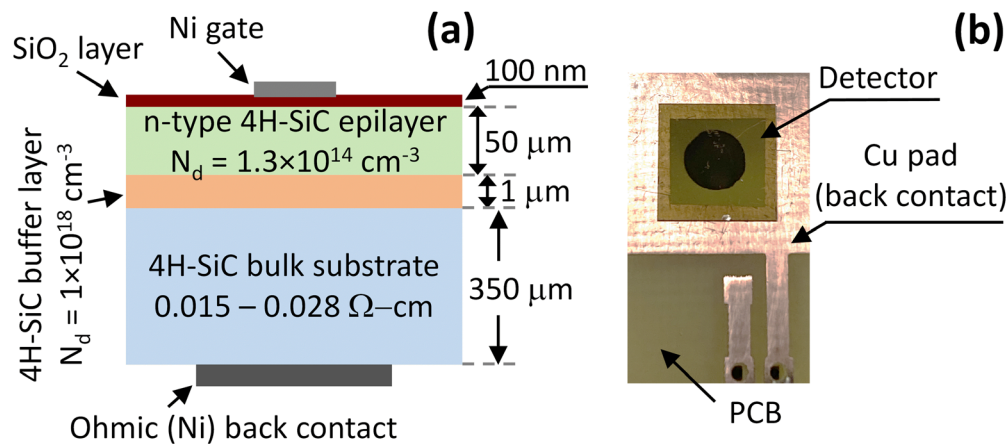


FIG. 1. (a) A cross-sectional schematic (not to scale) of the MOS detector structure. The SBD structure is similar except for the absence of the SiO_2 layer. (b) Photograph of a MOS detector mounted on a PCB that has been used in this study. The circular top nickel gate and the square back contacts are also visible. The top gate contact arm has not been shown to ensure clarity of the picture.

the 4H-SiC epilayer.^{21,22} Recently, vertical MOS capacitor detectors,²³ a variant of the SBD configuration, have been demonstrated to exhibit very high energy resolution (0.4% for 5486 keV alpha particles) as well.²⁴ Thin interfacial oxide layers preserve the Schottky diode type nature of the junction to maintain low leakage currents at operating bias while keeping the bulk and surface leakage currents low. Regardless of the detector configuration, the energy resolution of the 4H-SiC detectors is limited by the intrinsic detector resolution, which among other factors is controlled by the charge trapping centers such as carbon vacancy related $\text{Z}_{1/2}$ and $\text{EH}_{6/7}$ centers.^{25–27} Thermal oxidation of 4H-SiC has been reported to reduce the concentration of the carbon vacancy defects in 4H-SiC;^{28,29} however, the role of such defect mitigation strategies in radiation detectors has not been studied yet.

Two square shaped wafers with an edge length of 8 mm were diced from the parent wafer, which is a CVD grown 50 μm thick 4H-SiC epitaxial layer on the (0001) face of a highly conducting 350 μm thick 4H-SiC bulk substrate and 4° offcut toward the $\langle 11\bar{2}0 \rangle$ direction. Circular ($\phi = 3.8$ mm) nickel contacts were deposited on the Si side of one of the wafers to obtain a Schottky barrier detector and on the silicon dioxide (SiO_2) surface grown on the other wafer to obtain the MOS capacitor. Figure 1(a) shows the schematic of the MOS device structure, where a SiO_2 layer is deposited on a 50 μm thick n-type 4H-SiC epitaxial layer. The ≈ 100 nm thick SiO_2 layer was grown through dry thermal oxidation at 1000 $^\circ\text{C}$ for 10 h under constant oxygen flow. For the thermal oxidation, the epilayer sample was placed inside a quartz tube inserted into an MTI Corporation, GSL-1100X tubular horizontal furnace. The temperature of the furnace was raised to 1000 $^\circ\text{C}$ at a ramp rate of 10 $^\circ\text{C}/\text{min}$ following which, high purity oxygen gas was flown through a quartz tube at a rate of ~ 8 ml/min. Figure 1(b) shows a photograph of the MOS device mounted on a PCB used for the electrical and radiation detection measurements. For the temperature dependent measurements, the bare devices were mounted inside a JANIS VPF800 liquid-nitrogen cooled cryostat controlled by a Lakeshore 335 temperature controller.

Figure 2 shows the variation of the capacitance-voltage (C-V) characteristics of MOS50 and SBD50 as a function of the negative (reverse) bias measured at a test frequency of 1 MHz. For the sake of

convenience, the terms forward and reverse will be used for positive and negative anode (gate) bias, respectively, for both the devices. The built-in/flatband potentials and the effective doping concentrations have been calculated from the linear fits of the Mott-Schottky plots following a capacitance model given below

$$\frac{1}{C^2} = \frac{2}{q\epsilon_{4\text{H-SiC}}N_{\text{eff}}} (V_{bi} - V). \quad (1)$$

In the aforementioned equation, q is the elementary charge, $\epsilon_{4\text{H-SiC}}$ is the electrical permittivity of 4H-SiC ($\sim 8.55 \times 10^{-13}$ F/cm), N_{eff} is the effective doping concentration, V_{bi} is the built-in/flatband potential, and V is the applied bias voltage. The N_{eff} has been calculated to be 1.1×10^{14} and $1.9 \times 10^{14} \text{ cm}^{-3}$ for MOS50 and SBD50, respectively. A flatband potential of 1.5 V and a built-in potential of 1.8 V have been calculated for MOS50 and SBD50, respectively.

Figure 3(a) shows the semi-logarithmic current-voltage (I - V) plots obtained for the MOS50 and SBD50 detectors measured in the

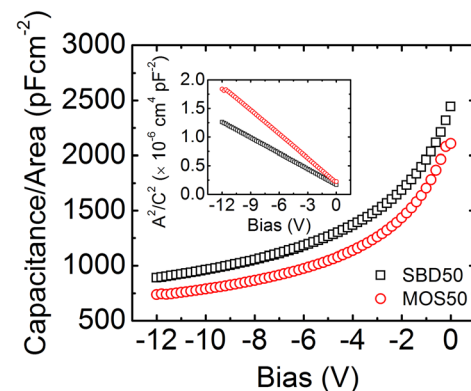


FIG. 2. Variation of device capacitance as a function of bias for a $\text{Ni}/\text{SiO}_2/\text{n-4H-SiC}$ MOS capacitor (MOS50) and a $\text{Ni}/\text{n-4H-SiC}$ Schottky barrier (SBD50) detector. The inset shows the corresponding Mott-Schottky plots.

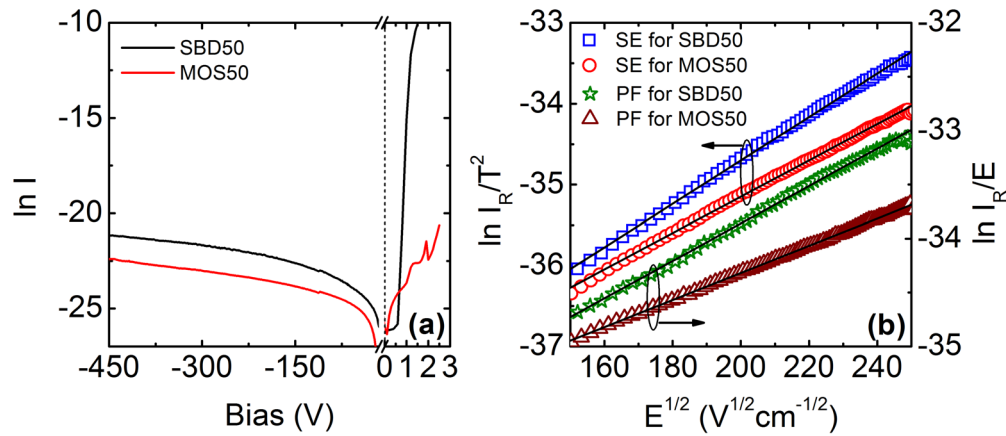


FIG. 3. (a) $\ln I$ vs V plot of MOS50 and SBD50 detectors measured at room temperature under the dark. (b) Electric field dependence of the reverse current following the Schottky emission (SE) and Poole-Frenkel emission (PF) model. The solid lines are the linear fit, and the dots represent the experimental data.

dark and at room temperature using a Keithley 237 source-measure unit. The SBD50 detector exhibited rectification behaviors with a rectification factor of $\approx 10^6$ at ± 1.6 V typically obtained in our high-resolution 4H-SiC SBD detectors. The voltage rate of increase in current in the positive gate bias region of MOS50 is lower than that of SBD50 in the forward bias region. A rectification factor of $\approx 10^2$ at ± 1.6 V was observed for MOS50. The relative lower rectification rate is expected as the presence of the interfacial oxide layer increases the series resistance of the MOS detector manifold compared to that of the SBD and limits the forward current. A positive gate voltage on the top Ni contact of the MOS detector rather causes accumulation of electrons at the Si/SiO₂ interface. The lower rectification factor, however, does not affect the detection properties as radiation detectors are operated in the depletion mode (negative gate bias), and as is evident from Fig. 3(a), the MOS50 detector exhibited much lower dark currents. In a metal-semiconductor (n-type) junction, the reverse leakage current, especially at high reverse bias, results due to the transport of electrons in the metal side that overcomes the barrier height and crosses to the semiconductor side. The observed increase in the reverse current I_R with increasing reverse bias results from the reduction of the barrier height with reverse bias and indicates toward field enhanced thermionic emission. Further information on the emission mechanism can be obtained from the slope of the linear fits to the $\ln(I_R/E)$ vs $E^{1/2}$ or $\ln(I_R/T^2)$ vs $E^{1/2}$ plots shown in Fig. 3(b).^{30–33} The electric field E is calculated as $E = qN_{\text{eff}}(V_R + V_{bi})/2\epsilon_{4H-\text{SiC}}$. The slope in both cases is given in (2), which can be used to determine if the emission is likely assisted by the Schottky effect (SE) or Poole-Frenkel (PF) effect

$$S = \frac{q}{mkT} \sqrt{\frac{q}{\pi\epsilon_{4H-\text{SiC}}}}. \quad (2)$$

In the above equation, m is equal to 1 or 2 depending on PF or SE mechanism, respectively. The plots corresponding to the SE and PF emissions for both detectors were found to be linear. The slope corresponding to the SE plot was calculated to be 0.02 and that for the PF plot was calculated to be 0.01 for both MOS50 and SBD50. The slopes were also calculated using (2) at $T = 300$ K and were found to be 0.02 and 0.006 for the SE and PF effects, respectively. Since the experimental and the calculated values of the slopes match very well for $m = 2$, it

indicates that the dominant mechanism of leakage current flow for both the detectors is Schottky emission. As the emission mechanism is similar in both detectors, the consistently lower leakage current observed for MOS50 compared to that of SBD50 is most likely because of the lower magnitude of the surface current due to the surface passivation through the SiO₂ layer.

Pulse-height spectroscopic measurements were carried out using a standard benchtop alpha spectrometer to evaluate the radiation detection response of the detectors coupled to a Cremat CR110 preamplifier. Figure 4 shows the variation of charge collection efficiency (CCE) η and energy resolution as a function of the bias voltage. The CCE has been calculated as the ratio of the detected and the incident alpha energy based on the pulse height spectra (PHS) obtained by exposing the detectors to a 0.9 $\mu\text{Ci}^{241}\text{Am}$ alpha emitting source. The energy resolution has been calculated as the full width at half maximum (FWHM) of the 5486 keV peak in the PHS and expressed as the percentage of the incident energy. Figures 5(a) and 5(b) show the PHS obtained for MOS50 and SBD50, respectively. The three alpha peaks

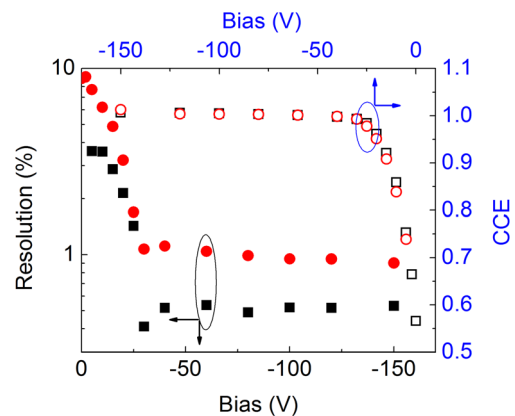


FIG. 4. Variation of percentage energy resolution and charge collection efficiency of the MOS50 and SBD50 detectors measured for 5486 keV alpha particles emitted by a ^{241}Am source as a function of the reverse bias voltage. The open and solid squares represent MOS50, and the open and solid circles represent SBD50.

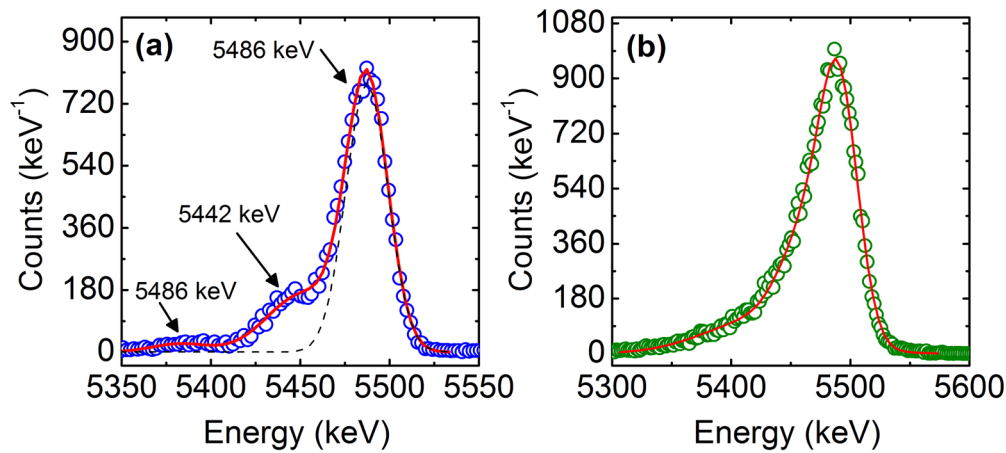


FIG. 5. Alpha pulse height spectra obtained for (a) MOS50 and (b) SBD50 using a ^{241}Am source. The lower energy alpha peaks were resolved by MOS50. The solid lines show the overall (multi-) Gaussian peak fits. The dashed line in (a) shows the Gaussian fit to the 5486 keV peak only.

α_1 , α_2 , and α_3 corresponding to the primary alpha peaks with energies 5486, 5443, and 5388 keV, respectively, were observed in the PHS of MOS50, which ensures a high energy resolution. The comparatively lower resolution of SBD50 is evident as the three alpha peaks were not resolved in the PHS. Both the detectors achieved the full CCE ($\eta = 1$) at around -30 V; however, the best energy resolutions (lowest FWHM) were obtained at -30 and -150 V for the MOS50 and SBD50 detectors, respectively, at a shaping time of $2 \mu\text{s}$, which were set as their optimized operating conditions. The energy resolution at the optimized settings were calculated to be 21 keV (0.4%) and 49 keV (0.9%) at 5486 keV for MOS50 and SBD50, respectively. The lower N_{eff} values obtained for the MOS50 detector partially account for the difference in the optimum operating bias. At -30 V, the depletion width of MOS50 is $\approx 18 \mu\text{m}$, which is the projected range of 5486 keV alpha particles in 4H-SiC, causing the incident alpha particles to stop within the depletion width. This above observation is consistent with the general observation that the optimized performance of Schottky barrier detectors is obtained when the majority fraction of the charge carriers is generated within the depletion width. Because of the higher N_{eff} value, the same depletion width is obtained at -60 V in SBD50. However, the observation that SBD50 required higher bias (-150 V) as the operating voltage indicates the influence of charge trapping. Repeated charge trapping in defects leads to poor charge transport, which may be overcome at higher bias voltages.

Since both the devices have been fabricated using wafers cut from the same parent wafer at nearby locations, the intrinsic parameters controlling the detector resolution, such as Fano factor, are likely to be same. On the contrary, the extrinsic parameters such as the electronic noise (controlled to a large extent by the device leakage current and capacitance), energy loss at the window, and experimental conditions such as source-detector geometry are kept strictly the same for both the detectors except for the unintentional difference in the detector capacitance and leakage current. The effect of these device parameters on the overall electronic noise and, hence, the detector energy resolution can be further analyzed following an equivalent noise charge (ENC) model given in (3).³⁴ The right side of (3) comprises the white series noise (WSN), pink noise (PN) (f parallel and $1/f$ series), and

white parallel noise (WPN). The ENC has been calculated as the width of a precision pulser peak in the PHS acquired under the same experimental conditions as set during the acquisition of the alpha PHS. Further details on the ENC model and the experimental method can be found in Ref. 24:

$$\text{ENC}^2 = (aC_{\text{tot}}^2 A_1) \frac{1}{\tau} + \left[\left(2\pi a_f C_{\text{tot}}^2 + \frac{b_f}{2\pi} \right) A_2 \right] + (bA_3)\tau. \quad (3)$$

In the aforementioned equation, τ is the amplifier shaping time constant, A_1 , A_2 , A_3 , a , a_f , and b_f are constants related to the shaping network response and the preamplifier components, and hence are same for both the detectors during the data acquisitions. The only parameters those are different for the two cases are b , which give the sum of the white parallel contribution due to the shot noise of the input field effect transistor (FET) and the detector leakage current, and C_{tot} , which is the total input capacitance expressed as the parallel combination of input test capacitance, stray capacitance, pre-amplifier feedback capacitance, the FET input capacitance, and the detector capacitance. Hence, the factors that control the WSN and PN are largely the detector capacitance, and the one controlling the WPN is the detector leakage current. Figure 6 shows the ENC squared plotted for both the detectors as a function of the shaping time τ . The plots have been fitted with (3) to derive the contribution of each noise term to the overall electronic noise. The variations of the WSN, PN, and WPN for both the detectors have also been plotted in Fig. 6. It is clear from the ENC analysis that the overall noise and the components are similar for both the detectors. The WPN was seen to be marginally lower in the case of the MOS50 detector compared to SBD50, which is consistent with the observed lower leakage current. However, the difference is too small to account for the observed difference in the energy resolution of the two detectors.

The above noise analysis and the related discussion rule out the effect of the extrinsic factors behind the lower resolution of the SBD50 and indicate toward the role of electrically active defects that participate in charge carrier trapping. A Sula Technologies, Inc., DDS-12 DLTS system operated in a capacitance mode has been used to characterize the defects and correlate with the device performance.¹⁴

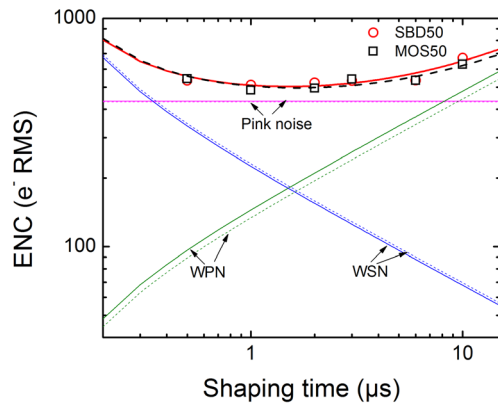


FIG. 6. Variation of equivalent noise charge (ENC) as a function of the amplifier shaping time with MOS50 and SBD50 coupled to a CR110 preamplifier and biased at -30 and -150 V, respectively. The dashed and solid lines represent the electronic noise components of MOS50 and SBD50, respectively.

Capacitance mode DLTS is a highly sensitive and accurate method for characterizing defects in rectifying devices.^{33,35} Figure 7(a) shows the DLTS spectra for the MOS50 and SBD50 detectors. The detectors were kept at a steady-state reverse bias of -12 V and pulsed to 0 V for a duration of 2 ms with a repetition rate of 1 Hz. Two well-defined peaks corresponding to electron traps were observed in the temperature scan range 240 – 750 K for each detector. The two trap centers observed in MOS50 and SBD50 are labeled as M1, M2 and S1, S2, respectively. At least four different rate windows have been used to obtain the Arrhenius plots corresponding to each peak observed in the DLTS spectra and are shown in Fig. 7(b). The trap parameters, calculated from the DLTS spectra and the Arrhenius plots, are given in Table I. The activation energies of M1 and S1, calculated with respect to the conduction band minimum, identify with the intrinsic $Z_{1/2}$ center related to carbon vacancies. The $Z_{1/2}$ centers are invariably present in CVD grown n-type 4H-SiC epilayers and are the primary electron trap centers responsible for deterioration of carrier lifetime.^{36–38} However, since the corresponding concentrations and capture cross

TABLE I. Trap parameters obtained from the DLTS measurements of a Ni/SiO₂/n-4H-SiC MOS capacitor and Ni/n-4H-SiC SBD.

Peak	ΔE (eV)	σ_n (10^{-15} cm ²)	N_t (10^{12} cm ⁻³)	Possible trap identity
M1	$E_C-0.68$	7.02	2.55	$Z_{1/2}$
M2	$E_C-1.10$	0.003	0.56	ON2/EH ₅
S1	$E_C-0.68$	6.7	1.97	$Z_{1/2}$
S2	$E_C-1.56$	5.82	0.11	EH _{6/7}

sections are found to be similar in both devices, the observed difference in the energy resolution between the two devices is unlikely to be due to the role of the $Z_{1/2}$ center. The different activation energies corresponding to peaks S2 and M2 imply that the peaks originate from different defect centers. The activation energy (1.56 eV) of the trap center S2 in SBD50 corresponds to the EH_{6/7} center, which is again related to carbon vacancies, and is commonly found in as-grown n-type 4H-SiC epilayers.^{39,40} An activation energy of 1.10 eV corresponding to the peak M2 has been attributed to the EH₅ center in n-type 4H-SiC by many authors.^{41,42} However, a defect with similar activation energy has been observed to emerge in n-type 4H-SiC after growing an SiO₂ layer through dry thermal oxidation and has been identified as ON2.^{28,29} The EH₅ center in 4H-SiC has been attributed to a carbon antisite vacancy (CAV) pair, where a carbon antisite (C_{Si}) couples with a neighboring carbon vacancy (V_C),^{43,44} whereas ON2 has been identified as interstitial type defects.^{29,37} Although the concentrations of the defects corresponding to peaks M2 and S2 are of the same order, the capture cross section corresponding to the M2 peak in MOS50 is orders of magnitude lower compared to that of S2 in SBD50. This implies that the electron trapping in the MOS50 detector is primarily at $Z_{1/2}$ centers, whereas in SBD50, an almost equal number of electrons are additionally trapped in the EH_{6/7} center. The substantial electron trapping in SBD50 accounts for its observed lower resolution.

The defect concentrations may vary spatially in a 4H-SiC parent wafer to some extent but the observation of different defect configurations in the MOS50 detector derived from the same parent wafer indicates the role of the growth of the SiO₂ layer. Thermal oxidation is

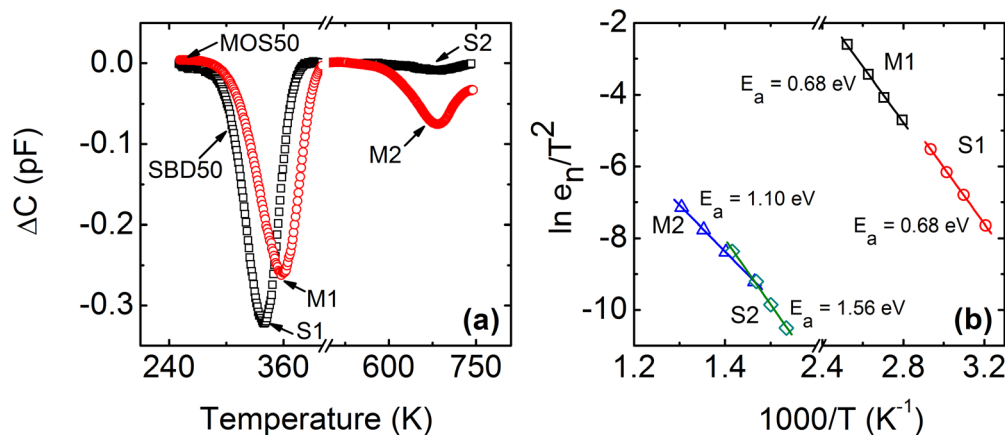


FIG. 7. (a) Capacitance mode DLTS scans for MOS50 and SBD50 detectors. (b) Arrhenius plots corresponding to the DLTS peaks. Solid lines show the linear fits. The corresponding activation energies have also been provided.

known to subdue carbon vacancy defects via a reported mechanism, where the excess carbon atoms at the interface diffuse into the epilayer and recombine with the carbon vacancies resulting in the reduction of both $Z_{1/2}$ and $EH_{6/7}$ concentrations in 4H-SiC.^{28,29} Interestingly, in the present study, the concentration of the $Z_{1/2}$ has been observed to remain practically unchanged. The authors, hence, propose that the high temperature oxidation process transforms the $EH_{6/7}$ defects to a new center through a multistep mechanism. For instance, Si emission during oxidation leads to the formation of silicon vacancies Si_V ,⁴⁵ which might turn into C_{Si} by capturing a carbon interstitial. The C_{Si} and the pre-existing carbon vacancies ($EH_{6/7}$) then form the CAV complex. Although conjectural, the above-mentioned possibility may address the outstanding questions related to the role of defect dynamics in the formation of CAV complexes, a highly sought-after spin-1/2 point defect that forms stable qubit states for quantum information processing and metrology.⁴⁶

This work was supported by the U.S. Department of Energy (DOE) Office of Nuclear Energy's Nuclear Energy University Program (NEUP), Grant No. DE-NE0008662. This work was also supported in part by the Advanced Support Program for Innovative Research Excellence-II (ASPIRE-II), Grant No. 80004453, and Support to Promote Advancement of Research and Creativity (SPARC) of the University of South Carolina (UofSC), Columbia, USA (Grant No. N1400-80004172).

AUTHOR DECLARATIONS

Conflict of Interest

The authors have no conflicts to disclose.

Author Contributions

OmerFaruk Karadavut: Data curation (equal); Formal analysis (equal); Investigation (equal); Methodology (equal); Writing – original draft (equal); Writing – review and editing (equal). **Sandeep K. Chaudhuri:** Conceptualization (equal); Data curation (equal); Formal analysis (equal); Investigation (equal); Methodology (equal); Writing – original draft (equal); Writing – review and editing (equal). **Joshua W. Kleppinger:** Formal analysis (equal); Investigation (equal); Methodology (equal); Writing – original draft (equal); Writing – review and editing (equal). **Ritwik Nag:** Data curation (equal); Formal analysis (equal); Investigation (equal); Methodology (equal); Writing – original draft (equal); Writing – review and editing (equal). **Krishna C. Mandal:** Conceptualization (lead); Data curation (supporting); Formal analysis (equal); Funding acquisition (lead); Investigation (equal); Methodology (equal); Project administration (lead); Resources (lead); Supervision (lead); Validation (supporting); Visualization (equal); Writing – original draft (equal); Writing – review and editing (equal).

DATA AVAILABILITY

The data that support the findings of this study are available from the corresponding author upon reasonable request.

REFERENCES

- ¹S. Das, T. Isaacs-Smith, A. Ayhi, M. A. Kuroda, and S. Dhar, *J. Appl. Phys.* **130**, 225701 (2021).

- ²F. Zhao, O. Amnuayphol, K. Y. Cheong, Y. W. Wong, J.-Y. Jiang, and C.-F. Huang, *Mater. Lett.* **245**, 174 (2019).
- ³S. Rakheja, K. Li, K. M. Dowling, A. M. Conway, and L. F. Voss, *IEEE J. Electron Devices Soc.* **9**, 521 (2021).
- ⁴A. Jayawardena, R. P. Ramamurthy, A. C. Ahly, D. Morissette, and S. Dhar, *Appl. Phys. Lett.* **112**, 192108 (2018).
- ⁵S. O. Kasap, M. Z. Kabir, K. O. Ramaswami, R. E. Johanson, and R. J. Curry, *J. Appl. Phys.* **128**, 124501 (2020).
- ⁶S. O. Kasap, K. O. Ramaswami, M. Z. Kabir, and R. Johanson, *J. Phys. D* **52**, 135104 (2019).
- ⁷G. Lioliu, A. B. Renz, V. A. Shah, P. M. Gammon, and A. M. Barnett, *Nucl. Instrum. Methods Phys. Res., Sect. A* **1027**, 166330 (2022).
- ⁸D. Puglisi and G. Bertuccio, *Micromachines* **10**, 835 (2019).
- ⁹P. G. Neudeck, D. J. Spry, M. J. Krasowski, N. F. Prokop, and L. Chen, *Mater. Sci. Forum* **963**, 813 (2019).
- ¹⁰F. H. Ruddy, L. Ottaviani, A. Lyoussi, C. Destouches, O. Palais, and C. Reynard-Carette, *EPJ Web Conf.* **253**, 11003 (2021).
- ¹¹S. K. Chaudhuri and K. C. Mandal, "Radiation detection using n-type 4H-SiC epitaxial layer surface barrier detectors," in *Advanced Materials for Radiation Detection*, edited by K. Iniewski (Springer, Cham, 2022), p. 183.
- ¹²Y. Hayashi, T. Mitani, N. Komatsu, T. Kato, and H. Okumura, *J. Cryst. Growth* **523**, 125151 (2019).
- ¹³F. Triendl, G. Pfusterschmied, G. Pobegan, S. Schwarz, W. Artner, J. P. Konrath, and U. Schmid, *Mater. Sci. Semicond. Process.* **131**, 105888 (2021).
- ¹⁴J. W. Kleppinger, S. K. Chaudhuri, O. F. Karadavut, R. Nag, and K. C. Mandal, *J. Cryst. Growth* **583**, 126532 (2022).
- ¹⁵J. W. Kleppinger, S. K. Chaudhuri, O. Karadavut, and K. C. Mandal, *J. Appl. Phys.* **129**, 244501 (2021).
- ¹⁶I. Capan, *Electronics* **11**, 532 (2022).
- ¹⁷G. Bertuccio, D. Puglisi, L. Torrisi, and C. Lanzieri, *Appl. Surf. Sci.* **272**, 128–131 (2013).
- ¹⁸S. K. Chaudhuri, K. J. Zavalla, and K. C. Mandal, *Appl. Phys. Lett.* **102**, 031109 (2013).
- ¹⁹A. Lo Guidice, F. Fizzotti, C. Manfredotti, E. Vittone, and F. Nava, *Appl. Phys. Lett.* **87**, 222105 (2005).
- ²⁰J. A. Cooper, Jr., *Phys. Status Solidi A* **162**, 305 (1997).
- ²¹K. C. Mandal, J. W. Kleppinger, and S. K. Chaudhuri, *Micromachines* **11**, 254 (2020).
- ²²S. K. Chaudhuri, K. J. Zavalla, and K. C. Mandal, *Nucl. Instrum. Method Phys. Res., Sect. A* **728**, 97 (2013).
- ²³Y. Jia, Y. Shen, X. Sun, Z. Shi, K. Jiang, T. Wu, H. Liang, X. Cui, W. Lü, and D. Li, *Nucl. Instrum. Methods Phys. Res., Sect. A* **997**, 165166 (2021).
- ²⁴S. K. Chaudhuri, O. Karadavut, J. W. Kleppinger, and K. C. Mandal, *J. Appl. Phys.* **130**, 074501 (2021).
- ²⁵J. W. Kleppinger, S. K. Chaudhuri, O. Karadavut, and K. C. Mandal, *Appl. Phys. Lett.* **119**, 063502 (2021).
- ²⁶T. Kobayashi, K. Harada, Y. Kumagai, F. Oba, and Y. Matsushita, *J. Appl. Phys.* **125**, 125701 (2019).
- ²⁷B. Zařko, F. Dubecký, A. řagátová, K. Sedlařková, and L. Rýč, *J. Instrum.* **10**, C04009 (2015).
- ²⁸K. Kawahara, J. Suda, and T. Kimoto, *J. Appl. Phys.* **111**, 053710 (2012).
- ²⁹K. Kawahara, J. Suda, and T. Kimoto, *Appl. Phys. Express* **6**, 051301 (2013).
- ³⁰C. R. Crowell and S. M. Sze, *Solid State Electron.* **9**, 1035 (1966).
- ³¹C. R. Crowell and M. Beguwalla, *Solid State Electron.* **14**, 1149 (1971).
- ³²H. Schroeder, *J. Appl. Phys.* **117**, 215103 (2015).
- ³³S. K. Chaudhuri, J. W. Kleppinger, and K. C. Mandal, *J. Appl. Phys.* **128**, 114501 (2020).
- ³⁴G. Bertuccio and A. Pullia, *Rev. Sci. Instrum.* **64**, 3294 (1993).
- ³⁵D. V. Lang, *J. Appl. Phys.* **45**, 3023 (1974).
- ³⁶I. Pintilie, L. Pintilie, and K. Irmscher, *Appl. Phys. Lett.* **81**, 4841 (2002).
- ³⁷K. Kawahara, X. T. Trinh, N. T. Son, E. Janzén, J. Suda, and T. Kimoto, *Appl. Phys. Lett.* **102**, 112106 (2013).
- ³⁸N. T. Son, X. T. Trinh, L. S. Løvlie, B. G. Svensson, K. Kawahara, J. Suda, T. Kimoto, T. Umeda, J. Isoya, T. Makino, T. Ohshima, and E. Janzén, *Phys. Rev. Lett.* **109**, 187603 (2012).
- ³⁹K. Danno, T. Kimoto, and H. Matsunami, *Appl. Phys. Lett.* **86**, 122104 (2005).

- ⁴⁰T. Hornos, A. Gali, and B. G. Svensson, *Mater. Sci. Forum* **679–680**, 261 (2011).
- ⁴¹R. Karsthof, M. E. Bathen, A. Galeckas, and L. Vines, *Phys. Rev. B* **102**, 184111 (2020).
- ⁴²H. Nakane, M. Kato, Y. Ohkouchi, X. T. Trinh, I. G. Ivanov, T. Ohshima, and N. T. Son, *J. Appl. Phys.* **130**, 065703 (2021).
- ⁴³I. Capan, T. Brodar, R. Bernat, Ž. Pastuović, T. Makino, T. Ohshima, J. D. Gouveia, and J. Coutinho, *J. Appl. Phys.* **130**, 125703 (2021).
- ⁴⁴N. T. Son, P. Stenberg, V. Jokubavicius, H. Abe, T. Ohshima, J. U. Hassan, and I. G. Ivanov, *Appl. Phys. Lett.* **114**, 212105 (2019).
- ⁴⁵C. J. Cochrane, P. M. Lenahan, and A. J. Lelis, *J. Appl. Phys.* **109**, 014506 (2011).
- ⁴⁶E. M. Y. Lee, *Nat. Commun.* **12**, 6325 (2021).